Applied Geochemistry 118 (2020) 104637

Contents lists available at ScienceDirect

Applied Geochemistry

journal homepage: http://www.elsevier.com/locate/apgeochem

Trace element composition of stibnite: Substitution mechanism and implications for the genesis of Sb deposits in southern China

Shanling Fu [a,b], Ruizhong Hu [a,c,*], Xianwu Bi [a], Neal A. Sullivan [b], Jun Yan [a]

[a] State Key Laboratory of Ore Deposit Geochemistry, Institute of Geochemistry, Chinese Academy of Sciences, Guiyang, 550081, China
[b] Department of Earth Sciences, University of Toronto, 22 Russell St., Toronto, ON, M5S 3B1, Canada
[c] College of Earth and Planetary Sciences, University of Chinese Academy of Sciences, Beijing, 100049, China

ARTICLE INFO

Editorial handling by Prof. M. Kersten

Keywords:
Trace element composition of stibnite
Substitution mechanism
Xikuangshan Sb deposit
Woxi
Genesis of Sb deposits

ABSTRACT

Though stibnite is among the most predominant Sb-bearing mineral phases in most Sb deposits, little is known about the trace elements and their substitution mechanism in stibnite that are valuable to better decipher the genesis of Sb deposits. This study determined quantitatively the trace element compositions of stibnite from two representative Sb deposits (Xikuangshan and Woxi) in southern China using high-resolution LA-ICP-MS. Results show that stibnite at Xikuangshan contains measurable Hg and As (typically 10–100 ppm); however, As, Cu, and Pb are the most abundant trace elements at Woxi (generally 100–500 ppm). Furthermore, the relatively smooth LA-ICP-MS profiles indicate As, Cu, and Pb primarily occurs as solid solution in stibnite. Hence the substitution $2Sb^{3+} \leftrightarrow Cu^{+} + Pb^{2+} + As^{3+}$ is likely responsible for the enrichment of Cu, Pb, and As in stibnite. Other trace elements, including Au, Ag, Bi, In, Mo, Sn, Co, Cr, V, Zn, Ni, Ga, Ge, Rb, Sr, Pd, Cd and U, are generally at concentrations of 0.01–1 ppm, with spiky LA-ICP-MS depth profiles, which are indicative of their presence as sparse micro-inclusions within stibnite. The apparent differences in trace element concentrations of stibnite suggest that the stibnite from two deposits may have been generated by different processes, or may reflect differences in fluid chemistry. The relative enrichment of As, Cu, and Pb indicate that the original Sb-bearing fluids for the Woxi deposit were likely enriched in these elements in the source region, but a geochemical segregation led to the formation of stibnite-dominated ores. In contrast, the monomineralic ores at Xikuangshan was likely originated from an initial absence of these elements in their source regions. The Hg/(Cu + Pb) ratio for the Xikuangshan Sb deposits is typically greater than 1 but the Woxi deposit tends to be much lower than 1. Therefore, the differences in trace element composition in stibnite can be useful to discriminate between Sb deposit types.

1. Introduction

The trace element composition of ore minerals is generally dependent of the fluid characteristics such as redox state, pressure, temperature, and the fluid source regions, and therefore has been widely used to elucidate the ore genesis and ore-forming processes for various hydrothermal deposits (Cook et al., 2009, 2012; Ciobanu et al., 2013; Johnson et al., 2013; Reich et al., 2013; George et al., 2015). Stibnite is a common constituent of hydrothermal mineralization in a range of ore systems; in particular, stibnite is the principal ore mineral in most Sb deposits (Dill et al., 2008; Hu et al., 2017; Chen et al., 2018; Li et al., 2018; Fu et al., 2019a, b) and the only Sb-bearing ore mineral in some Sb deposits (e.g., Xikuangshan Sb deposit; Peng et al., 2003a). However, little has been done in previous studies toward characterizing the elemental composition of stibnite. In particular, to our knowledge, very few studies (Cook et al., 2013) have been concerned with the trace element composition of stibnite in a quantitative manner. Therefore, a comprehensive study of the trace elemental composition of stibnite is valuable for potentially elucidating the ore genesis of Sb deposits.

The Xiangzhong metallogenic province (XZMP) in southern China hosts more than 100 Sb deposits, which constitutes more than 50% of the world's Sb production and current reserves (Hu and Zhou, 2012; Hu et al., 2017), and thus provides an ideal location for investigating trace element compositions of stibnite. The Sb deposits in this region can be classified into two groups based on metal association as well as host rocks and spatial distribution: (i) Devonian to Carboniferous sediment-hosted, intrusion-distal deposits located within the Xiangzhong basin (Wu, 1993; Ma et al., 2003 ; Peng et al., 2003a; Fan et al.,

* Corresponding author. State Key Laboratory of Ore Deposit Geochemistry, Institute of Geochemistry, Chinese Academy of Sciences, Guiyang, 550081, China.
E-mail address: huruizhong@vip.gyig.ac.cn (R. Hu).

https://doi.org/10.1016/j.apgeochem.2020.104637
Received 18 March 2020; Received in revised form 30 April 2020; Accepted 9 May 2020
Available online 19 May 2020

2004; Yang et al., 2006a); (ii) Pre-Devonian metamorphic rock-hosted deposits located in the Xuefengshan uplift belt (Peng and Frei, 2004; Gu et al., 2007, 2012; Liang et al., 2014 ; Zhu and Peng, 2015). The former group is characterized by stibnite as the only ore mineral without a polymetallic contribution and is best represented by the Xikuangshan Sb deposit (Hu et al., 1996; Peng et al., 2003a; Fan et al., 2004; Hu and Peng, 2018). The latter one is characterized by Sb and associated polymetallic mineralization where the ore minerals include stibnite, native gold, pyrite, arsenopyrite and scheelite, such as the Woxi Sb–Au–W deposit, Longshan Sb–Au deposit, and Zhazixi Sb–W deposit (Peng and Frei, 2004; Zhu and Peng, 2015; Zeng et al., 2017a, b; Zhang et al., 2014). While a range of studies have focused on these Sb deposits for decades, their genesis is still debated and various genetic models have been proposed linking the two deposit styles orogenic, epithermal, intrusion-related, and even SEDEX deposits (Liu et al., 1985; Mao and Li, 1997; Peng and Frei, 2004; Gu et al., 2007, 2012; Dill et al., 2008; Zhu and Peng, 2015). Xikuangshan and Woxi are the largest and most representative Sb deposits of Sb-only and Sb-polymetallic deposits in the world, respectively, where stibnite is the predominant ore mineral and thus are appropriate for investigating trace element compositions of stibnite.

Xikuangshan is the most representative Sb-only deposit, which has a total Sb metal reserve of up to 2.5 Mt with an average grade of about 4.0% Sb (Kuang, 2000; Hu et al., 2017). Woxi is the most important Sb-polymetallic deposit in the XZMP, with contained Au, Sb, and WO_3 metal reserves amounting to >50 t, ~2.2 Mt, and 25,000 t, respectively, and average ore grades of Au, Sb, and W of 9.8 g/t, 2.8%, and 0.3%, respectively (Zhu and Peng, 2015). This paper reports a LA-ICP-MS study of trace element composition in stibnite from the two giant Sb deposits in the XZMP of southern China. The objectives of this study are (i) to provide quantitative data for trace element compositions of stibnite, (ii) to unravel the element distribution and the substitution mechanism of trace elements in stibnite, and (iii) to place new constraints on the ore fluid origin and genetic processes. Although the findings of our study are preliminary and warrant verification by additional studies, we believe that the trace element composition of stibnite

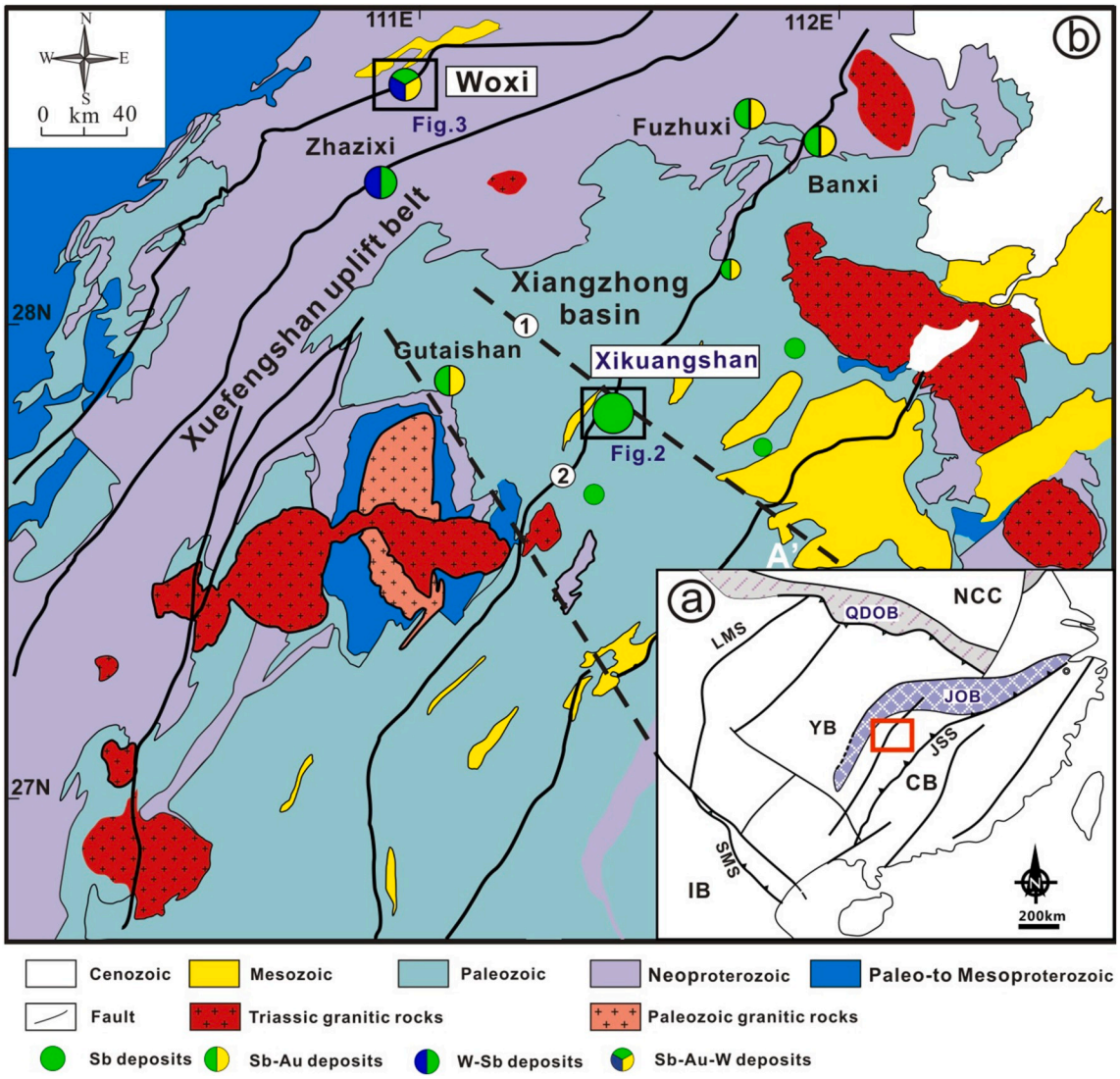

Fig. 1. (a) Tectonic framework of South China Block including the location of Xiangzhong Metallogenic Province (central Hunan) (Modified from Qiu et al., 2016; Hu et al., 2017); (b) regional geological map of the Xiangzhong Sb–Au metallogenic province in southern China, including the distribution of important Sb deposits (Modified from BGMRHN, 1988; Xie et al., 2019). CB-Cathaysia Block; IB-Indochina Block; JOB-Jiangnan Orogen Belt; JSS-Jiang-Shao Suture; LMS-Longmenshan Fault; NCC-North China Craton; QDOB-Qinling-Dabie Orogen Belt; SMS-Song-Ma Suture; YB-Yangtze Block; ①-Xikuangshan-Lianyuan Fault; ②-Chengbu-Taojiang Fault.

can provide useful information for elucidating the ore genesis and even provide useful information for mineral exploration of Sb deposits.

2. Regional and deposit geology

The South China Block is composed of the Yangtze Block and Cathaysia Block, which were amalgamated along the Jiangshao suture zone during Neoproterozoic (Zhao et al., 2011a; Yao et al., 2016, Fig. 1a). The XZMP is located in the eastern part of the Yangtze Block (Fig. 1a) and consists of the Xiangzhong basin and Xuefengshan uplift belt (Fig. 1b). The basement of this region comprises low-grade metasedimentary rocks of Late Proterozoic and Early Paleozoic age, whereas the overlying non-metamorphosed sedimentary rocks consist of mainly Upper Paleozoic to Mesozoic carbonate and clastic rocks (BGMRHN, 1988; Ma et al., 2002). This region was intruded by late Triassic granitic rocks, and to a less extent, by Paleozoic granitoids along the margin of Xiangzhong basin (Fig. 1b), of which were interpreted to be produced by the partial melting of Proterozoic metasedimentary rocks (Chu et al., 2012; Fu et al., 2015; Xie et al., 2019).

As described above, more than 100 Sb-bearing deposits and occurrences have been found in the Xuefengshan Uplift Belt and the adjacent Xiangzhong Basin (Hu et al., 2017). These Sb deposits can be divided into two groups: Sb-only deposits and Sb-polymetallic deposits. The Xikuangshan and Woxi are the largest and most representative ones of these two types of Sb deposits in this region. Their geological features have been described in previous literature (Hu et al., 1996; Peng et al., 2003a; Fan et al., 2004; Gu et al., 2007, 2012; Zhu and Peng, 2015; Hu and Peng, 2018; Fu et al., 2019a, b), and details of the most important features are summarized below.

2.1. Xikuangshan Sb deposit

The Xikuangshan deposit is located at the intersection of the Taojiang-Chengbu and Xikuangshan-Lianyuan regional faults within the Xiangzhong basin (Fig. 1b). Strata exposed in the Xikuangshan district including Devonian Xikuangshan and Shetianqiao Formations, and Carboniferous Datang and Yanguan Formations (Fig. 2a), are dominated by carbonates interbedded with siltstone, argillite, and shale/mudstone (Hu et al., 1996; Peng et al., 2003a). The Sb orebodies are dominantly hosted in the central portion of the Devonian Shetianqiao Formation (D_3s^2), and to a lesser extent, in the lower part (D_3s^1). The D_3s^2 is composed of sandstone, carbonate and shale/mudstone layers from the bottom to the top, with a total thickness of >350 m. The shale/mudstone layer above the carbonate layer was thought to have acted as a barrier to ascending ore fluids (Jin et al., 2001; Yang et al., 2006b). Structurally, the deposit is strictly confined within the Xikuangshan complex anticline, and the sub-anticlines of this complex anticline controlled the occurrence and distribution of orebodies and formed four ore blocks (Peng et al., 2003a, Fig. 2a). This complex anticline was cut by several NE-trending faults. Among these faults, the F_{75} fault cuts the northwest limb of the anticline, which is believed to have been the main channel for migrating ore fluids (Liu and Jian, 1983). A NE-trending lamprophyre dike with a calc-alkaline affinity is the only intrusive rock at Xikuangshan (Wu and Hu, 2000; Xie et al., 2001, Fig. 2a). Though the precise age remains unclear, the dike is believed to postdate the Sb mineralization of the Xikuangshan deposit (Hu and Peng, 2016).

Orebodies at Xikuangshan are controlled by the secondary interlayer fractures associated with the F_{75} fault, and are chiefly stratiform in shape, and therefore parallel host strata of Devonian age. In addition to stratiform veins, high-angle veins and vein networks, and irregular veinlets are also identified (Peng et al., 2003a; Hu and Peng, 2018). The orebodies generally extend from 30 m to 600 m along strike and 1300–1800 m down dip with a thickness of 1–5m (locally up to 20 m) (Kuang, 2000). The mineral assemblage of ores is monotonous with stibnite, the only economic mineral, and gangue consisting of quartz and calcite in variable proportions; minor fluorite, barite, and gypsum are also present (Hu et al., 1996; Peng et al., 2003a; Hu and Peng, 2018). Based on mineral paragenesis, three stages of mineralization are recognized, i.e., pre-ore, ore-forming, and post-ore (Hu et al., 2017; Hu and Peng, 2018). Ore-hosting carbonate rocks are highly silicified, and the distribution of all Sb orebodies does not appear to exceed the limit of silicic alteration (Kuang, 2000, Fig. 2b).

Though no sophisticated model has been proposed to fully explain the formation of Xikuangshan deposit, available fluid-inclusion data show that the ore fluids had epithermal temperatures of 150–250 °C and salinities <5 wt % NaCl equiv. (Lin, 2014; Hu and Peng, 2018). The data from hydrothermal calcite Sm–Nd dating and (U–Th)/He dating of zircon in altered wall rocks suggest that mineralization occurred in the Mesozoic (~150–120 Ma; Peng et al., 2003a; Fu et al., 2019a). More recently, Fu et al. (2019b) proposed a new model that invoked deep-circulation of meteoric water that mobilized Sb and S from basement metamorphic rocks underlying the Xiangzhong basin, ascended along regional faults F_{75}, and subsequently deposited Sb metals within favorable structural traps leading to the formation of this deposit.

2.2. Woxi Sb–Au–W deposit

The Woxi deposit is situated in the center of the Xuefengshan uplift (Fig. 1b). The strata exposed in the Woxi district mainly consist of the Proterozoic Lengjiaxi and Banxi Groups (Fig. 3a). The Lengjiaxi Group is exposed mainly in the southwest and southeast parts of the Woxi district and is mainly composed of epimetamorphic gray-green sandstones, siltstones, slates, and tuffaceous slates. The Banxi Group dominates in the middle and northern parts of the district and is composed of flysch consisting of slate and phyllite interbedded with local meta-volcanic materials (Luo et al., 1984). This group can be subdivided into the Madiyi Formation and Wuqiangxi Formation, which are separated by the EW-trending Woxi thrust fault. Mineralization is generally confined in the purplish-red calcareous sericite slate of Madiyi Formation, and is controlled by interlayer faults (Peng and Frei, 2004; Gu et al., 2012, Fig. 3b). The Woxi deposit contains five ore blocks from west to east: Hongyanxi, Yuershan, Lijiaxi, Shiliupenggong, and Shangwoxi (Fig. 3a). The Woxi thrust fault is the most important structure in the Woxi district, of which all orebodies occur in the footwall of this fault (Fig. 3b). No intrusive rocks have been identified in the Woxi district.

Orebodies at Woxi primarily occur as banded quartz veins parallel to bedding, and subordinately as bedding-discordant sheeted quartz veins, stockworks, and veinlets (Gu et al., 2012; Zhu and Peng, 2015 and pictures therein). Economically, the banded veins contribute about 70% of the total proven metal reserves and comprise a series of banded ore layers localized within different stratigraphic horizons of the Madiyi Formation. Compared to Xikuangshan, the mineral assemblage of ores in the Woxi deposit is more complex, with major metallic minerals including stibnite, pyrite and scheelite, and gangue minerals dominated by quartz, with minor calcite, dolomite, and chlorite. However, the mineral assemblages in separate ore blocks are diverse, and detailed mineralogical features and paragenesis of Woxi deposit have been previously documented by several researchers (Shao et al., 1996; Zhang et al., 2014; Zhu and Peng, 2015 and figures therein). It is worth noting that, the Shangwoxi ore block studied here is characterized by a simple ore composition of stibnite-quartz. Fluid-inclusion data suggest that this deposit was generated by low temperature (140–240 °C), low salinity (<7.0 wt % NaCl equiv.), CO_2-rich, N_2-bearing ore-forming fluid (Zhu and Peng, 2015). Alterations related to mineralization are dominated by silicification and sericitization. Although several attempts have been done to determine the mineralization age of Woxi deposit, equivocal results were obtained by different dating methods, ranging from *ca.* 145 Ma by quartz Rb–Sr dating (Shi et al., 1993) to *ca.* 400 Ma by scheelite Sm–Nd and quartz Ar–Ar dating (Peng et al., 2003b). Regarding genetic models, several viewpoints had been proposed including (i) SEDEX origin (Gu et al., 2007, 2012), (ii) magmatic hydrothermal origin (Mao and Li, 1997; Peng and Frei, 2004), and (iii) metamorphic hydrothermal

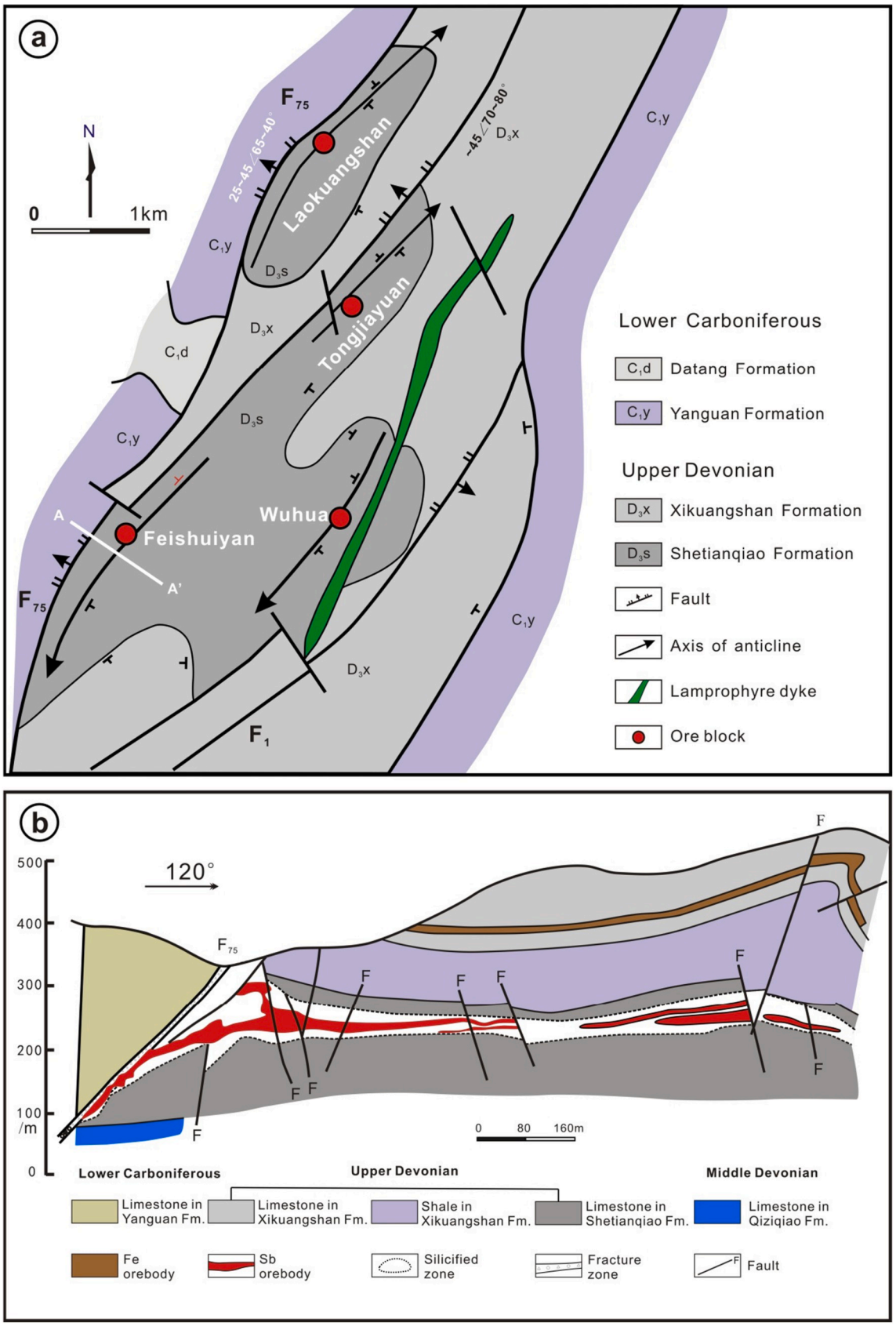

Fig. 2. (a) Geological map of the Xikuangshan giant Sb deposit in central Hunan, showing the locations of four ore blocks (i.e., Laokuangshan, Tongjiayuan, Feishuiyan and Wuhua) (Modified after from Peng et al., 2003a); (b) a typical profile map of the Xikuangshan Sb deposit, showing the occurrence of orebodies and its relationship with silicic alteration (Modified after Jin, 2002; Tao et al., 2002).

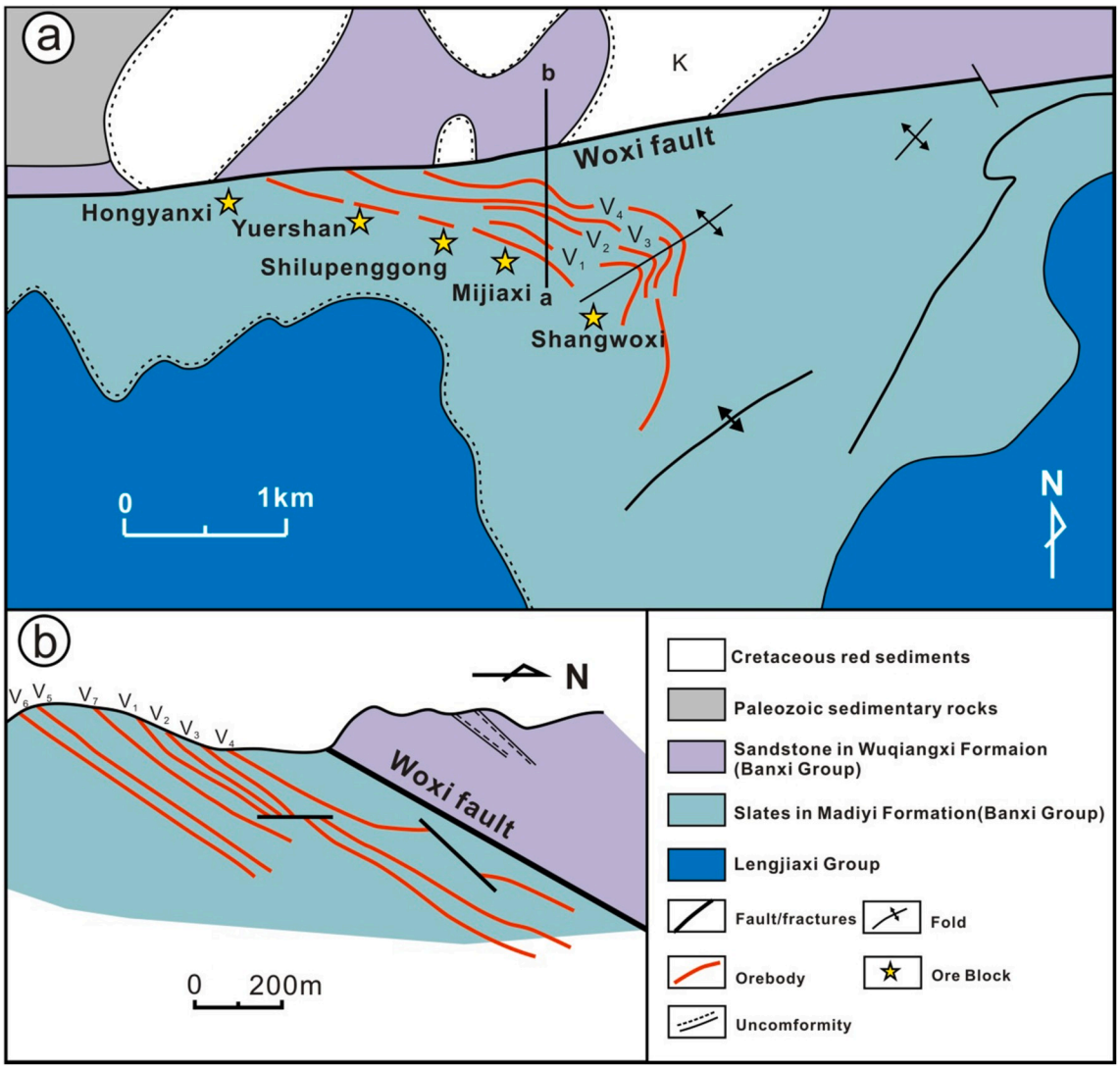

Fig. 3. (a) Geological map of the Woxi Sb–Au–W deposit, showing the locations of five ore blocks (Hongyanxi, Yuershan, Lijiaxi, Shiliupenggong, and Shangwoxi) (Modified after Peng and Frei, 2004); (b) a typical profile map of the Woxi deposit, showing the occurrence of mineralized quartz veins (Modified after Luo et al., 1984).

origin (Luo et al., 1984; Yang, 1992; Zhu and Peng, 2015).

3. Samples and analytical methods

A total of 39 stibnite-rich samples were collected from underground workings at Xikuangshan and Woxi deposits, and the details of samples are given in Table 1. Samples from Xikuangshan are generally massive but locally disseminated and stockwork. Three types of ores occur at Xikuangshan: (i) quartz-stibnite ore, (ii) calcite-quartz-stibnite ore, and (iii) calcite-stibnite ore (Fig. 4). As documented by Gu et al. (2007) and Zhu and Peng (2015), ores from different ore blocks at Woxi contain distinct mineral assemblages but, the Shangwoxi block is the major Sb producer and contains stibnite as the most important ore mineral (locally with trace scheelite). Therefore, samples of the Woxi deposit were mainly collected from different mining levels at the Shangwoxi block. It should be stressed that, similar to those of the Xikuangshan deposit, all the Woxi samples collected host a simple ore composition of stibnite as the major ore mineral and quartz as the principal gangue mineral (Table 1 and Fig. 5).

3.1. EPMA analyses

Electron microprobe analyses (EPMA) of stibnites was carried out on standard polished sections, and the areas of interest were delineated by the use of reflected light microscopy and were marked and photographed before analyzing. Major and minor element compositions of stibnite were determined using a Shimadzu EPMA-1720 electron microprobe. The operating conditions of the electron microprobe employed an accelerating voltage of 15 kV, a probe current of 20 nA and a beam diameter of 20 μm. For elemental calibration, various sulfides or synthetic metals were used as standards: Sb_2S_3 (Sb), FeS_2 (S, Fe), $FeAsS_2$ (As), Au–Ag (Au), $CuFeS_2$ (Cu), PbS (Pb) ZnS (Zn) and HgS (Hg). Matrix corrections were carried out using the ZAF correction program supplied by the manufacturer Shimadzu. Analytical errors are about 1% for major elements and 3% for minor elements.

3.2. LA-ICP-MS analyses

Quantitative trace element concentrations for stibnite were obtained using an Agilent 7700x Quadrupole ICP-MS coupled with a New Wave UP213 laser ablation system at the Institute of Geochemistry, Chinese

Table 1
Description of stibnite samples collected from the Xikuangshan Sb and Woxi Sb–Au–W deposits in southern China.

Deposits	Sample No.	Locality (elevation)	Mineral assemblage	Textures
Xikuangshan	XKS-2-2	Level 2#, +320 m	Stibnite + quartz + talc	Massive, breccia
Sb deposit	XKS-2-4		Stibnite + minor quartz	Massive
	XKS-3-3	Level 3#, +300 m	Stibnite + quartz	Massive
	XKS-3-4		Stibnite + quartz	Massive, breccia
	XKS-3-5		Stibnite + quartz	Massive
	XKS-3-8		Stibnite + quartz	Breccia
	XKS-4-1	Level 4#, +300 m	Stibnite + minor quartz	Massive, radial
	XKS-7-6	Level 7#, +190 m	Stibnite + quartz	Breccia
	XKS-9-3	Level 9#, +170 m	Stibnite + quartz + calcite	Massive, breccia
	XKS-9-5		Stibnite + quartz	Massive
	XKS-11-1	Level 11#, +136 m	Stibnite + quartz	Breccia, disseminated
	XKS-11-3		Stibnite + quartz + calcite	Massive
	XKS-13-5	Level 13#, +78 m	Stibnite + quartz + calcite	Breccia
	XKS-13-8		Stibnite + quartz + calcite(+talc)	Massive, breccia
	XKS-15-1	Level 15#, +30 m	Stibnite + calcite + quartz	Massive
	XKS-21-2	Level 21#, −34 m	Stibnite + calcite	Massive
	XKS-23-2	Level 23#, −120 m	Stibnite + quartz	Massive, breccia
	XKS-23-8		Stibnite + calcite	Vein, network-like
	XKS-25-2	Level 25#, −142 m	Stibnite + calcite + quartz	Breccia
Woxi Sb–Au–W deposit	WX-31-1	Level 31#, −485 m	Stibnite + quartz + pyrite	Massive
	WX-31-2		Stibnite + quartz	Massive (+veined)
	WX-31-3		Stibnite + quartz	Massive
	WX-32-1	Level 32#, −510 m	Stibnite + quartz	Massive (+veined)
	WX-32-2		Stibnite + quartz	Massive
	WX-32-3		Stibnite (+minor quartz)	Massive
	WX-32-4		Stibnite + quartz + pyrite	Veined
	WX-32-5		Stibnite + quartz	Massive
	WX-34-1	Level 34#, −560 m	Stibnite + quartz + scheelite	Veined
	WX-32-2		Stibnite + quartz	Massive
	WX-34-3		Stibnite + quartz + scheelite	Massive
	WX-34-4		Stibnite + quartz	Veined
	WX-34-5		Stibnite (+minor quartz)	Massive
	WX-34-6		Stibnite + quartz	Massive, veined
	WX-34-7		Stibnite (+minor quartz)	Massive
	WX-34-8		Stibnite + quartz	Massive
	WX-34-9		Stibnite + quartz	Massive
	WX-34-10		Stibnite + quartz	Massive, disseminated
	WX-34-11		Stibnite + quartz	Massive
	WX-34-12		Stibnite + quartz	Massive

Academy of Sciences. Laser ablation was carried out in a pure He atmosphere (0.48 L/min) using an in-house small-volume sample cell and the aerosol was mixed with Ar as a transport gas (0.9 L/min) immediately after leaving the cell. The measurement of stibnite spots was performed at 10 Hz laser pulse frequency and 40 μm spot size with laser energy of 3.5 J/cm^2. Analysis time for each spot was 120 s, comprising a 30-s measurement of background with laser off, and 60-s analysis with laser on, and followed by a 30-s retention time to ensure a proper cell washout. Batches of 10–15 analyses were bracketed by repeat analyses of the external standards, allowing monitoring of, and correction for, instrumental drift. A linear drift correction based on the analysis sequence and on the bracketing analyses of MASS-1 was applied to the count rate for each sample. Measured isotopes were selected to avoid isobaric and polyatomic interferences, and the following isotopes were measured: ^{7}Li ^{27}Al, ^{29}Si, ^{34}S, ^{51}V, ^{53}Cr, ^{55}Mn, ^{57}Fe, ^{59}Co, ^{60}Ni, ^{65}Cu, ^{66}Zn, ^{71}Ga, ^{72}Ge, ^{75}As, ^{77}Se, ^{85}Rb, ^{88}Sr, ^{95}Mo, ^{105}Pd, ^{107}Ag, ^{111}Cd, ^{115}In, ^{118}Sn, ^{125}Te, ^{197}Au, ^{201}Hg, ^{205}Tl, ^{208}Pb, ^{209}Bi and ^{238}U. The dwell time was set to 10 ms for each element measured, with a total sweep time of <0.5 s. Time-resolved LA-ICP-MS signals that showed clear peaks or strong rises (possible mineral or fluid inclusions) were discarded and the smooth time-resolved depth spectra can therefore represent an averaging effect due to the limited depth resolution. The external calibration was performed against the in-house standards (GSE-1G and GSD-1G), and sulfide reference material MASS-1 (formerly known as PSD-1; Wilson et al., 2002) was used as a secondary check (running as an "unknown") to monitor the analytical accuracy. The raw analytical data in each spot is plotted as a time-resolved depth spectrum and the integration time for background and sample signal selected. The counts are then corrected for instrument drift and converted to concentration values using the Sb values known from prior EMPA analyses as an internal standard. The synthetic standard glasses NIST SRM 610 and 612 (Pearce et al., 1997) were additionally measured to recognize a possible instrumental drift. Analytical accuracy for most elements is expected to be better than 20% with variations in spot size being the main additional contributing factor.

Additionally, to image trace element distribution within stibnite grains, a set of touching parallel lines arranged in a grid was ablated using a beam size of 10 μm. Rastering speed for each line was equal to the beam size per second (i.e., 10 μm/s). A set of nine elements was chosen for image analysis (As, Au, Ag, Hg, Cu, Pb, Zn, Fe, and Sb). Acquisition time was set to 6 ms for most elements, except Au (9 ms), and Ag (9 ms), resulting in a total sweep time of ~0.3 s. Raw effective image resolution along each line is ~2 times beam diameter. The complete maps were generated throughout 2–3 h to keep instrument drift in sensitivity to the minimum.

4. Results

4.1. Mineral chemistry of stibnite

A total of 14 representative stibnite-quartz ore samples, six from Xikuangshan and eight from Woxi, were analyzed by EPMA. As shown in Table 2, stibnites from two deposits host highly consistent major contents, i.e., S and Sb vary from 27.68% to 28.39% and 71.56%–73.44%, respectively. Although previously reported data suggested that stibnite could accommodate many elements (such as Fe, As, Pb, Au) to thousands

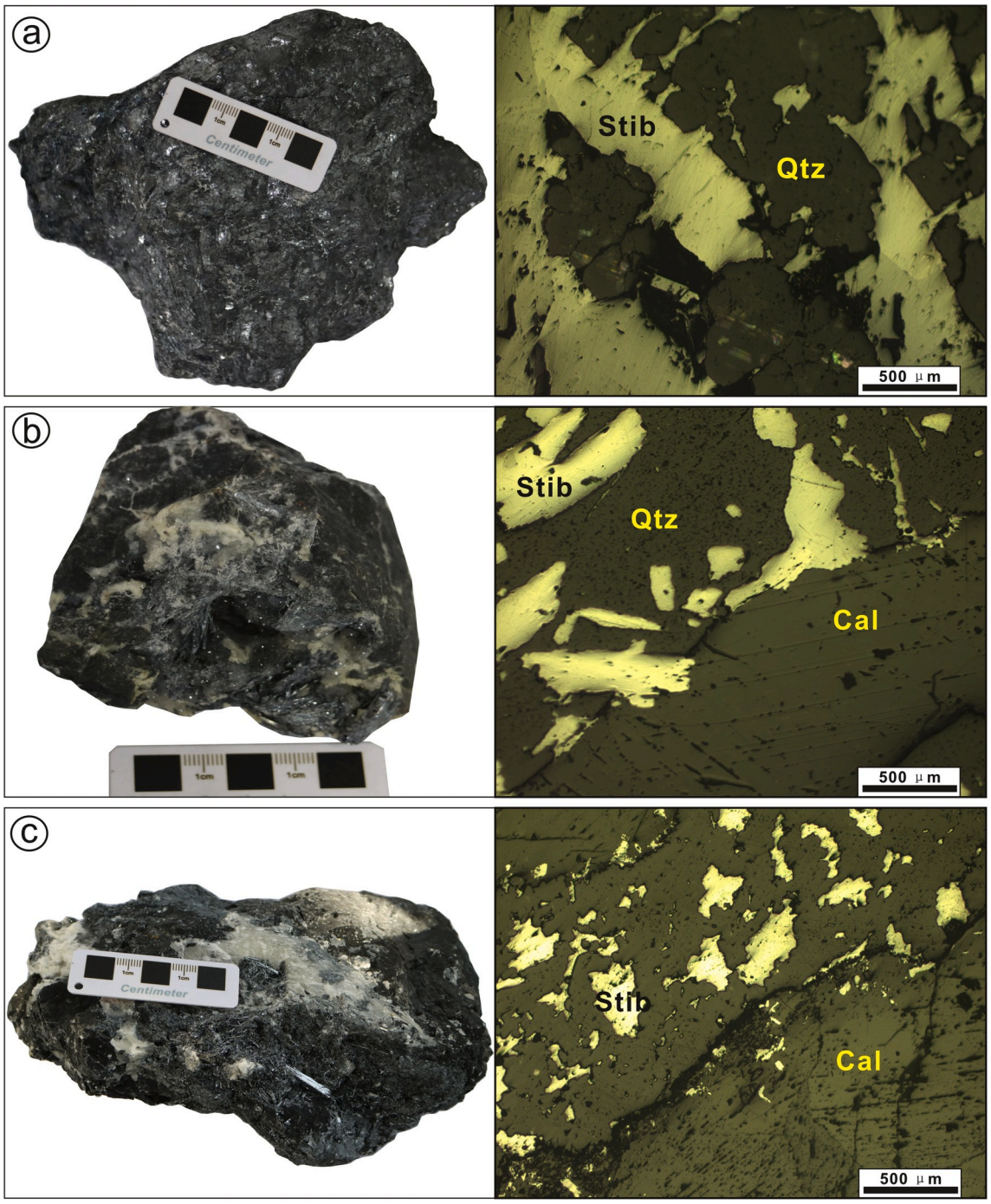

Fig. 4. Hand specimen and reflected light microphotographs of ores at the Xikuangshan Sb deposit. (a) Quartz-stibnite ores collected from the mining level 3#; (b) quartz-calcite- stibnite ores with disseminated fine-grained pyrites collected from the mining level 13# and (c) calcite-stibnite ore collected from the mining level 21#. Cal: Calcite; Qtz: Quartz; Py: Pyrite; Stib: Stibnite.

of ppm or even wt. % level (; Dickson et al., 1975; Watling et al., 1995; Murao et al., 1999; Hampton et al., 2004), elements (reported as minor elements in stibnite) including As, Au, Cu, Pb, Zn, Fe, and Hg analyzed in the present study were below their respective detection limits (0.04% or 400 ppm) using EPMA and thus no useable minor element data were obtained.

4.2. Trace element composition of stibnite

A total of 198 LA-ICP-MS spot analyses were acquired on 39 representative stibnite samples from two deposits, including 19 samples from the Xikuangshan deposit and 20 samples from the Woxi deposit. Since many elements were detected at extremely low concentrations or even below detection limits, here we just include the mean concentrations of a few elements with elevated concentrations as shown in Fig. 6, but report statistical data (mean, standard deviations, minimum and maximum concentrations) and entire LA-ICP-MS dataset in Electronic Supplementary Table S1 and Table S2, respectively. Despite our efforts to avoid visible inclusions, some analyses did show anomalous concentrations which may be a result of the presence of mineral or fluid inclusions (e.g., Fe- and Mn-rich inclusions). Identification of inclusions was determined by spot analyses that were inconsistent with stibnite.

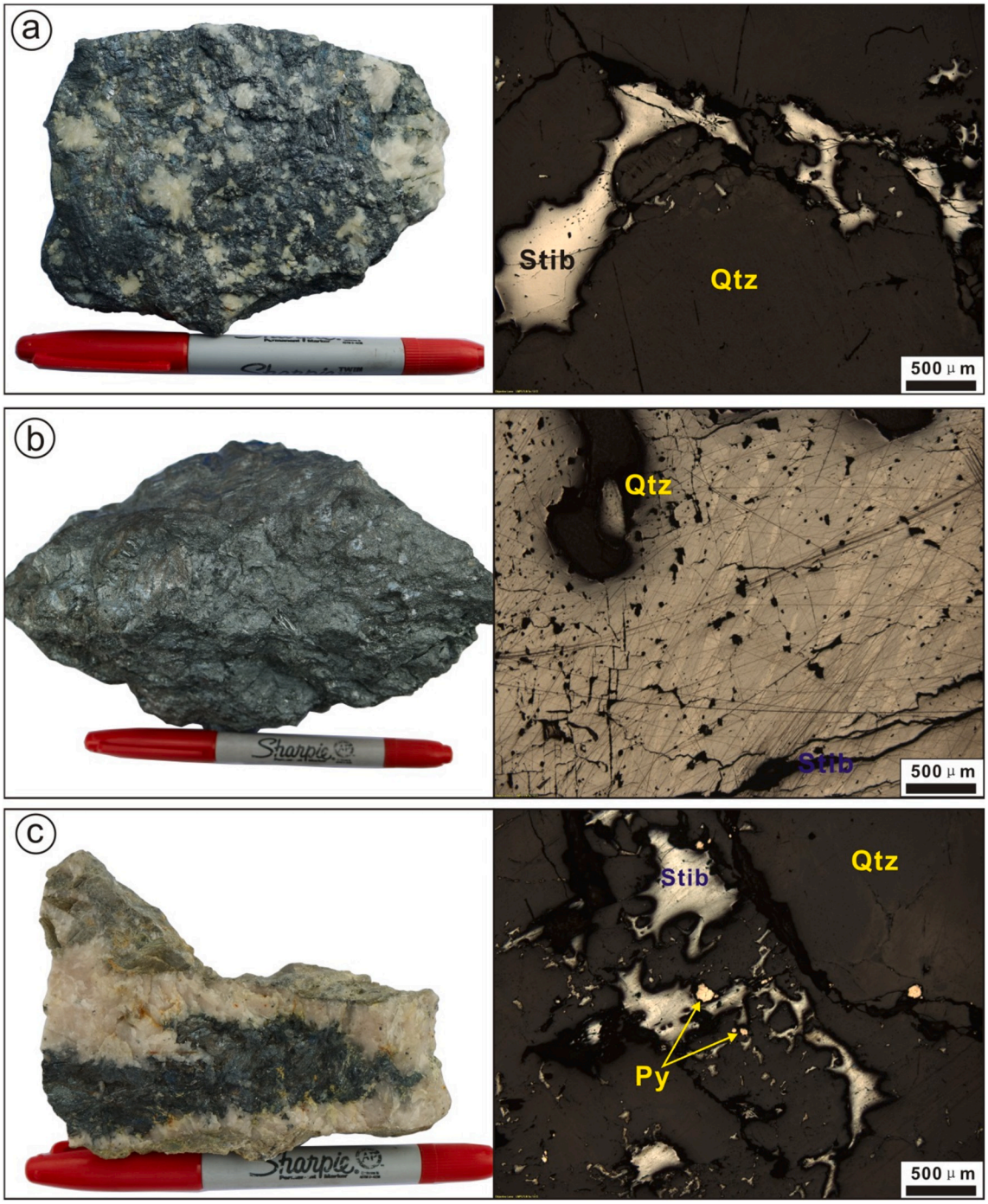

Fig. 5. Hand specimen and reflected light microphotographs of ores at the Woxi Sb–Au–W deposit. (a) Massive quartz-stibnite ores; (b) fine-grained quartz-stibnite aggregates; (c) veined quartz-stibnite with sparse pyrites. Cal: Calcite; Qtz: Quartz; Py: Pyrite; Stib: Stibnite.

The statistical calculations did not include these analyses inferred to contain inclusions.

The mean concentrations of major trace elements in individual samples from both deposits are plotted in Fig. 6, which allows visualization for both the range of absolute values for each element and the variance within each deposit. Overall, As, Cu, Pb, Hg, Fe, Zn, Se, and Te are the most abundant trace elements in stibnite. However, stibnite from different deposits has distinct trace element compositions. Arsenic is measurable in stibnite for both deposits but, the As concentration at Woxi deposit (typically >100–300 ppm) is generally one to two orders of magnitude higher than that of the Xikuangshan deposit (typically at 1–10 ppm; Fig. 6). In addition to As, the Cu and Pb concentrations at Woxi, varying within the range of tens to hundreds of ppm, are much higher than those of the Xikuangshan deposit that are commonly at the level of 0.01–10 ppm (Fig. 6). In contrast, Hg is significantly enriched in stibnite from the Xikuangshan deposit with concentration at tens to hundreds of ppm, whereas Hg in stibnite from Woxi deposit is typically at levels of 0.01–10 ppm. The Zn concentrations for stibnite from the Xikuangshan deposit is also relatively high and variable (typically at 0.1–100 ppm) compared to that of the Woxi deposit, which varies from 0.1 to 10 ppm. Additionally, the Fe, Se, and Te concentrations in stibnite from two deposits are comparable, with value for Fe and Te in the range of 1–100 ppm but, Te contents are lower, from 0.1 to 10 ppm (Fig. 6). Other trace elements in stibnite such as Au, Ag, Bi, In, Mo, Sn, Co, Cr, V,

Table 2
Electron microprobe analytical data of stibnites from the Xikuangshan Sb and Woxi Sb–Au–W deposits in southern China.

Deposits	Samples	Analyses	S/%	Sb/%	Total/%
Xikuangshan Sb deposit	XKS-2-2	X-2-2-1	28.13	72.60	100.73
		X-2-2-2	28.10	72.39	100.49
		X-2-2-3	27.92	72.63	100.56
	XKS-3-7	X-3-7-1	27.98	72.18	100.16
		X-3-7-2	28.00	71.62	99.62
		X-3-7-3	27.68	72.43	100.11
	XKS-4-3	X-4-3-1	27.93	72.65	100.58
		X-4-3-2	28.09	72.82	100.92
		X-4-3-3	27.88	72.69	100.57
	XKS-7-4	X-7-4-1	28.39	72.77	101.16
		X-7-4-2	27.80	72.61	100.41
		X-7-4-3	28.03	72.70	100.73
	XKS-11-3	X-11-3-1	28.39	72.44	100.83
		X-11-3-2	28.02	72.38	100.40
		X-11-3-3	28.14	72.72	100.86
		X-11-3-4	28.00	72.42	100.42
	XKS-13-8	X-13-8-1	27.96	72.23	100.19
		X-13-8-2	28.22	72.45	100.67
		X-13-8-3	28.08	72.34	100.43
		X-13-8-4	27.84	72.59	100.44
Woxi Sb–Au–W deposit	WXK-31-1	W-31-1-1	27.72	71.56	99.28
		W-31-1-2	27.79	72.09	99.88
	WXK-31-2	W-31-2-1	27.80	72.43	100.23
		W-31-2-2	28.08	72.50	100.58
	WXK-31-3	W-31-3-1	27.80	72.28	100.08
		W-31-3-2	28.19	73.44	101.63
		W-31-3-3	28.21	73.01	101.22
	WXK-32-1	W-32-1-1	28.06	72.63	100.69
		W-32-1-2	27.95	72.35	100.31
		W-32-1-3	27.98	72.75	100.73
	WXK-32-2	W-32-2-1	28.10	72.81	100.91
		W-32-2-2	28.15	72.90	101.05
		W-32-2-3	28.10	72.57	100.67
	WXK-34-1	W-34-1-1	28.13	72.62	100.75
		W-34-1-2	27.89	72.85	100.74
	WXK-34-2	W-34-2-1	28.04	72.56	100.60
		W-34-2-2	28.13	72.77	100.90
		W-34-2-3	28.34	73.19	101.53
	WXK-34-3	W-34-3-1	28.02	72.84	100.86
		W-34-3-2	28.09	72.74	100.82
		W-34-3-3	28.30	72.76	101.07

Ni, Ga, Rb, Sr, Pd, Cd, and U, compare similarly between deposits but have extremely low concentrations, which are typically on the order of 0.01–0.1 ppm (Fig. 6 and Table S2).

In addition to spot analyses, trace element distribution within stibnite grains from two types of Sb deposits was imaged by LA-ICP-MS. Fig. 7 shows the distribution of most abundant trace elements within stibnite grain from the sample XKS-3-4 collected at the level 3$^{\#}$ (elevation of +300 m) at Xikuangshan deposit, and no obvious grain-scale compositional zoning was observed.

5. Discussion

5.1. Trace element distribution in stibnite

Previous studies suggest that trace elements in sulfide minerals (e.g., pyrite, sphalerite, galena) generally occur as (i) solid solution or nanoparticles in crystal lattice; (ii) micro-inclusions; or (iii) visible fluid or mineral inclusions (Cook et al., 2009; Deditius et al., 2011; Ciobanu et al., 2013; Zhang et al., 2014; George et al., 2015). A careful inspection of LA-ICP-MS output signals from each laser spot analyses was done to discriminate between whether a particular trace element occurs as homogeneous solid solutions, or as larger isolated micro-inclusions. In general, a relatively flat time-resolved depth profile suggests that the associated trace element is either in solid solution or included as nanoparticles within the mineral structure (Genna and Gaboury, 2015; Dehnavi et al., 2018); while elements with spiky depth profiles typically indicate the presence of micro-scale inclusions carrying these elements (Cook et al., 2009; Ciobanu et al., 2013). Representative single-plot LA-ICP-MS depth profiles of major trace elements in stibnite are presented in Fig. 8, which can serve as key evidence for the trace element distribution in stibnite. In this study, the LA-ICP-MS depth profiles for As, Cu, Pb and Hg are relatively smooth or consist of a series of peaks of varying, but comparable, size (Fig. 8a and b), suggesting that these elements may primarily occur as solid solution within the crystal lattice or at least as invisible nanoparticles in stibnite. However, the high variability between individual spots and irregular depth profiles for such Fe and Mn (Fig. 8c) imply that these elements may be present in both solid solution and as micro-inclusions in stibnite. Element mapping also suggests that part of the Fe in stibnite can be present as isolated Fe-rich inclusions (Fig. 7). The LA-ICP-MS depth profiles for remaining trace elements including Au, Ag, Zn, Mo, Bi, Sn, Cr, V, Ni, Sr, Se, Te, Ge, Ga, Cd and U, generally show pronounced spikes, indicating that these elements primarily occur as micro-inclusions in stibnite (Zhao et al., 2011b; Deol et al., 2012).

Additionally, unlike other sulfide minerals, such as, pyrite, arsenopyrite, sphalerite and galena that often display grain-scale compositional zoning (Hinchey et al., 2003; Di Benedetto et al., 2005; Large et al., 2009; George et al., 2015), we did not observe any zoned distribution of trace elements in stibnite (Fig. 7). However, the trace element composition in stibnite from different deposits shows significant difference. For example, stibnite from the Woxi Sb–Au–W deposit is relatively enriched in Cu and Pb but depleted in Hg, with the Hg/(Cu + Pb) ratio typically lower than 1, while stibnite in the Xikuangshan deposit are relatively enriched in Hg but depleted in Cu and Pb with Hg/(Cu + Pb) ratios generally much greater than 1. The difference in trace element composition between deposits implies that stibnite from two deposits may be distinct in origin, or have been generated by different processes.

5.2. Element correlation and substitution mechanisms

Since the majority of measured trace elements in stibnite are below or slightly above minimum detection limits, the following discussion is focused on the correlation and substitution mechanisms for those trace elements with elevated concentrations well above the limits of detection. Considering the mean for each sample in the full dataset, Fig. 9a reveals a marked positive correlation (R = 0.95) between Cu and Pb in stibnite. This positive correlation implies that there must be an underlying factor governing the distribution of the two elements in stibnite, which is expected to be the result of the coupled substitution $Cu^{+}+Pb^{2+}\leftrightarrow Sb^{3+}$. This correlation is best observed where the Cu and Pb in stibnite are at elevated concentrations (>100 ppm) for the Woxi deposit (Fig. 9a). In an ideal coupled substitution, the Cu and Pb would be present in stibnite in an equal proportion. However, data obtained in this study show that mol% Cu is slightly higher that mol% Pb in stibnite (~1.2:1). This implies that the Cu, in addition to being incorporated in the crystal lattice via the substitution of $Cu^{+}+Pb^{2+}\leftrightarrow Sb^{3+}$, may also occur as micro-inclusions in stibnite. Element mapping also revealed the presence of isolated Cu-rich inclusions in stibnite (Fig. 7). In addition, it should be noted that, the presence of Cu in the 1+ oxidation state within the above substitution was assumed based on its presence in other common sulfide minerals such as chalcopyrite, sphalerite and galena (Goh et al., 2006; Cook et al., 2012; George et al., 2015), and thus further work needs to be done to validate the presence of Cu^{+} in stibnite. Therefore, it is plausible to propose that the substitution of Sb^{3+} by $Cu^{+}+Pb^{2+}$ is the dominant mechanism responsible for the enrichment of Cu and Pb into stibnite.

The full LA-ICP-MS dataset reveals several additional correlations between different element couples (Fig. 9b–d). For example, a weak positive correlation between Hg and Fe in stibnite at Xikuangshan deposit (R = 0.66; Fig. 9b) was observed, with a slope of ~2, implying that these two elements might be involved in a coupled substitution. Since both Hg and Fe are primarily present as solid solution within stibnite, it

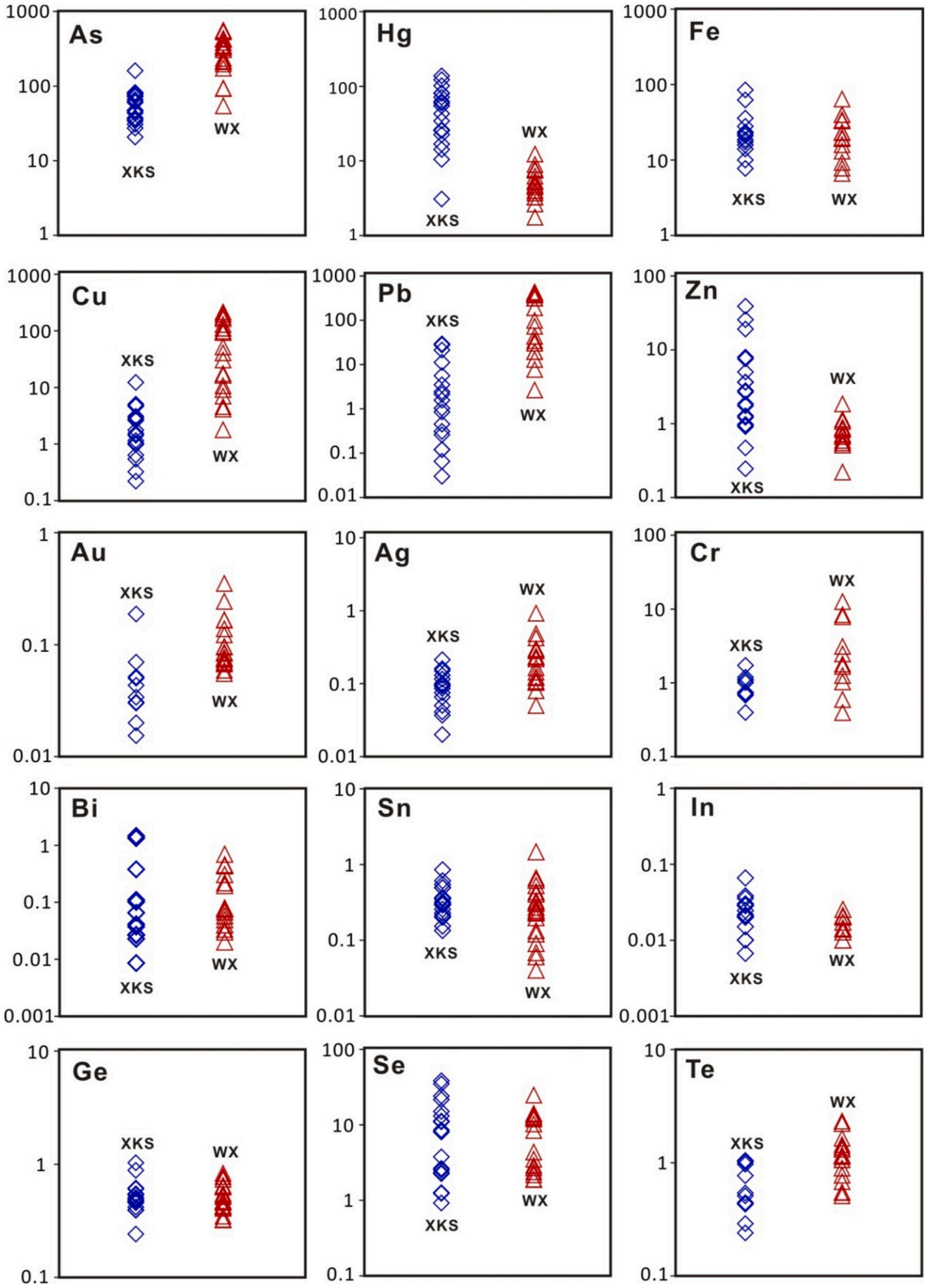

Fig. 6. Scatter plots showing the mean concentrations of key elements in stibnite determined by LA-ICP-MS. XKS: Xikuangshan Sb deposit, WX: Woxi Sb–Au–W deposit. All values in ppm.

can be presumed that the coupled substitution $2Sb^{3+} \leftrightarrow 2Hg^{2+} + Fe^{2+}$ may be the major factor governing the correlation between Hg and Fe. However, since such a trend is relatively weak as the distribution of Fe in stibnite is inhomogeneous, further work is needed to verify this substitution. Other correlations such as Sn *vs* Te in the Xikuangshan deposit (Fig. 9c), and Se *vs* Te in the Woxi deposit (Fig. 9d) were also observed. Nevertheless, the substitution mechanism for these elements remains unclear because these elements are generally at low concentrations of a few parts per million and are interpreted to be primarily present as micro-inclusions in stibnite.

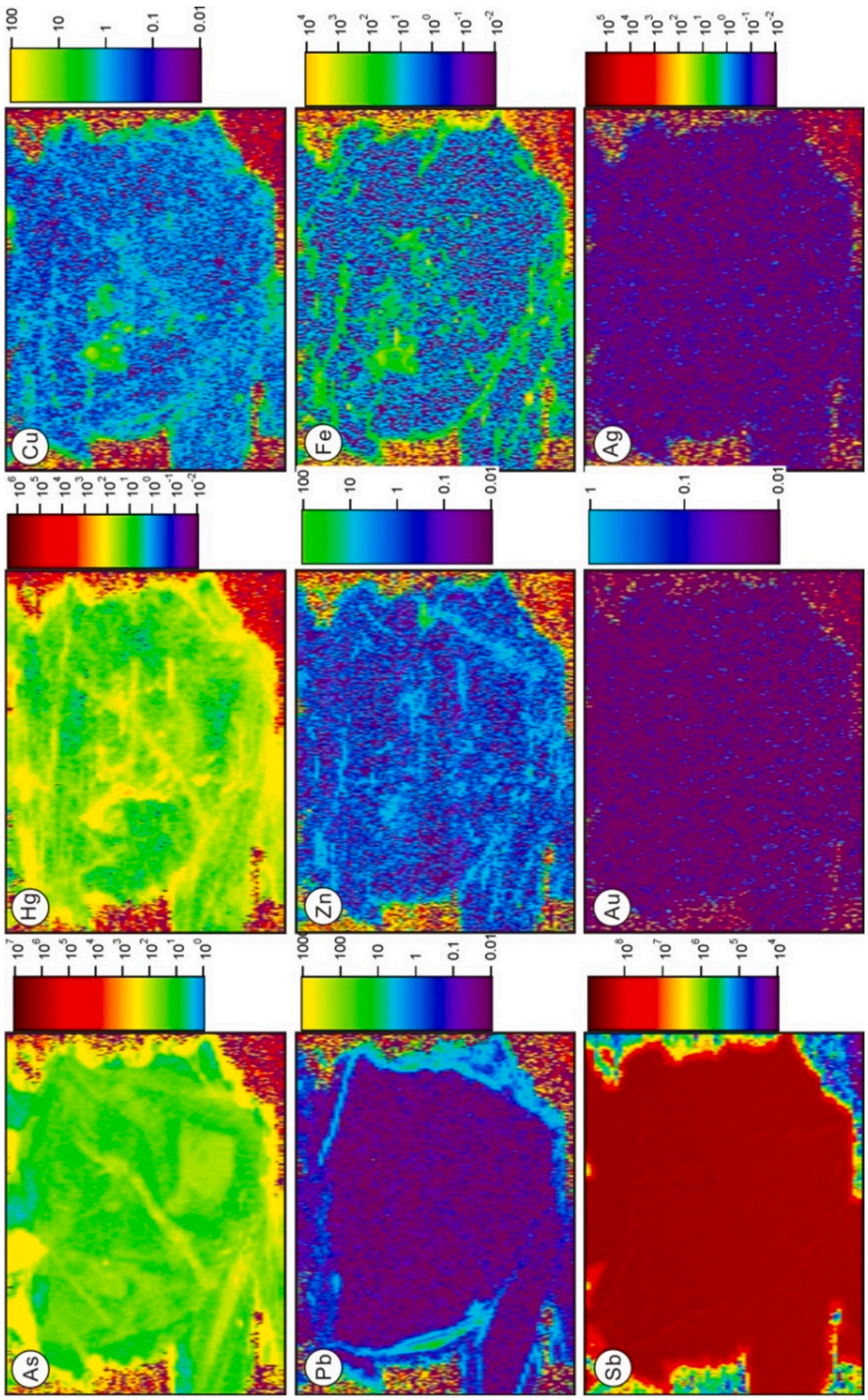

Fig. 7. LA-ICP-MS images of trace element distribution ((in counts per second) in stibnite from Sample XKS-3-4 in the Xikuangshan Sb deposit.

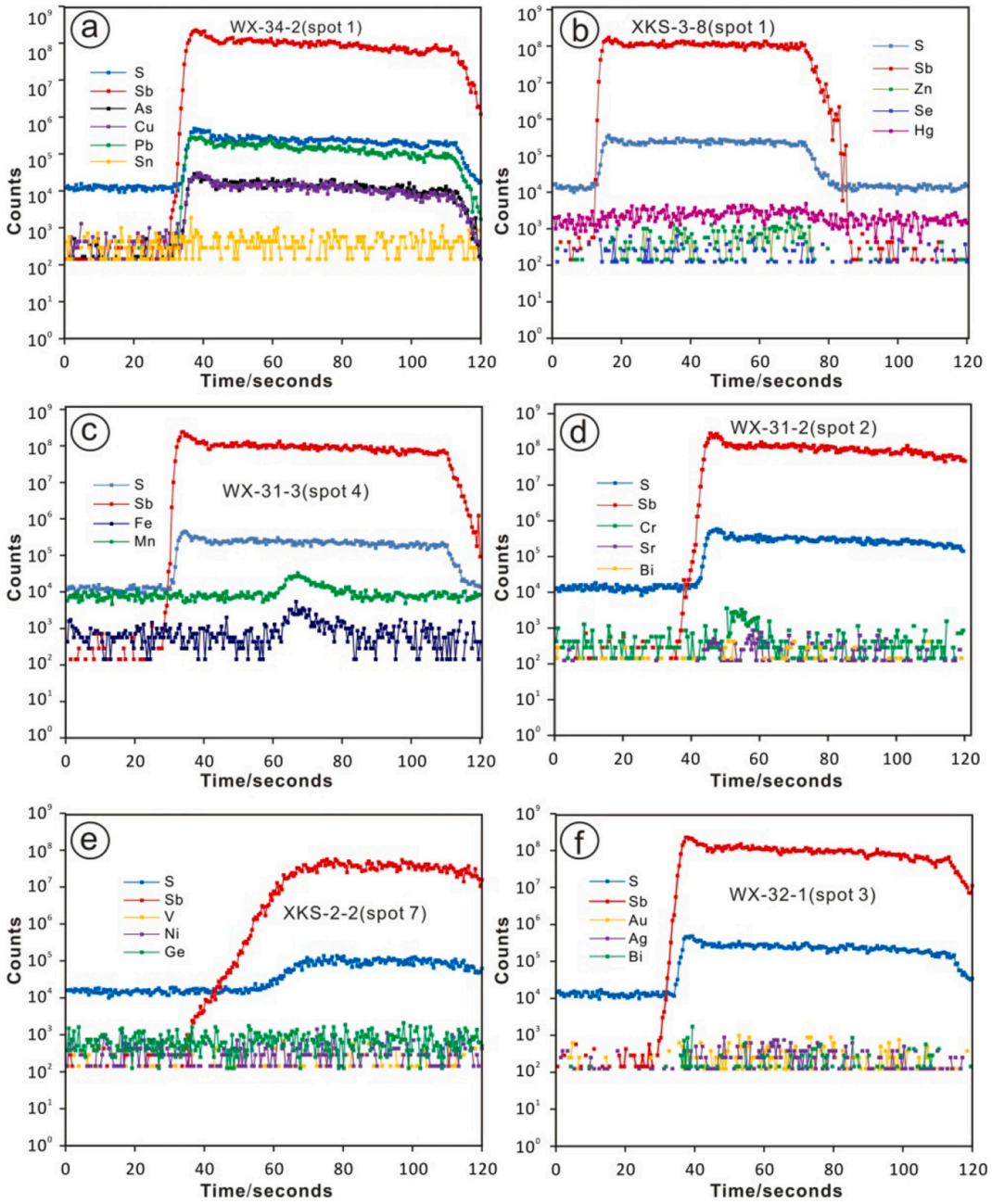

Fig. 8. Representative single-spot LA-ICP-MS depth profiles of selected elements in stibnite. Signals of As, Cu, Pb and Hg are relatively flat and consist of comparable peaks, implying that they may occur as solid solutions; whereas those of Au, Ag, Zn, Mo, Cr, Ni, C, Se, Sn, Bi, Sr and Ge show pronounced spikes, suggesting they may be present as micro-inclusions. However, the features of signals for Fe and Mn indicate that there may be Fe- and Mn-rich mineral inclusions beneath the sample surface.

It is notable that As is the most abundant trace element in stibnite, in particular for the Woxi deposit (generally >100–300 ppm); however, our results show that As does not have any discernible positive or negative correlation with any of the other trace elements analyzed. However, since As and Sb are similar in ionic radii and chemical property (Rytuba, 2003; Wilson et al., 2010) and both occur as solid solution in stibnite (Figs. 7 and 8), it is reasonable to speculate that the substitution of $2Sb^{3+}$ by $Cu^{+}+Pb^{2+}+As^{3+}$, or the simple substitution of Sb^{3+} by As^{3+} is likely responsible for the incorporation of As into stibnite for both deposit types.

5.3. *Implications for ore genesis of Sb deposits*

A variety of studies suggest that the majority of global Sb deposits generally host a monotonous mineral association with stibnite as the principal ore mineral (Gokce and Spiro, 1994; Dill et al., 1997, 2008; Peng et al., 2003a; Chen et al., 2018; Fu et al., 2019a,b). For example, although the Woxi is a Sb-polymetallic (Sb–Au–W) deposit, the Sb mineralization is often present separately from the W and Au mineralization, and produces a simple ore composition in the Shangwoxi ore block. However, the cause of essentially a monomineralic nature of stibnite ores in various deposit types remains unclear. Stanton (1972) proposed that the nearly complete absence of coevally deposited base-metal sulfide minerals in Sb deposits may have resulted from two potential mechanisms: (i) a simple lack of base-metals in source areas available for uptake into a Sb-bearing fluid; and (ii) a geochemical segregation or partitioning of base-metals from Sb-bearing fluids at depth through precipitation of higher P-T sulfides. The data obtained in

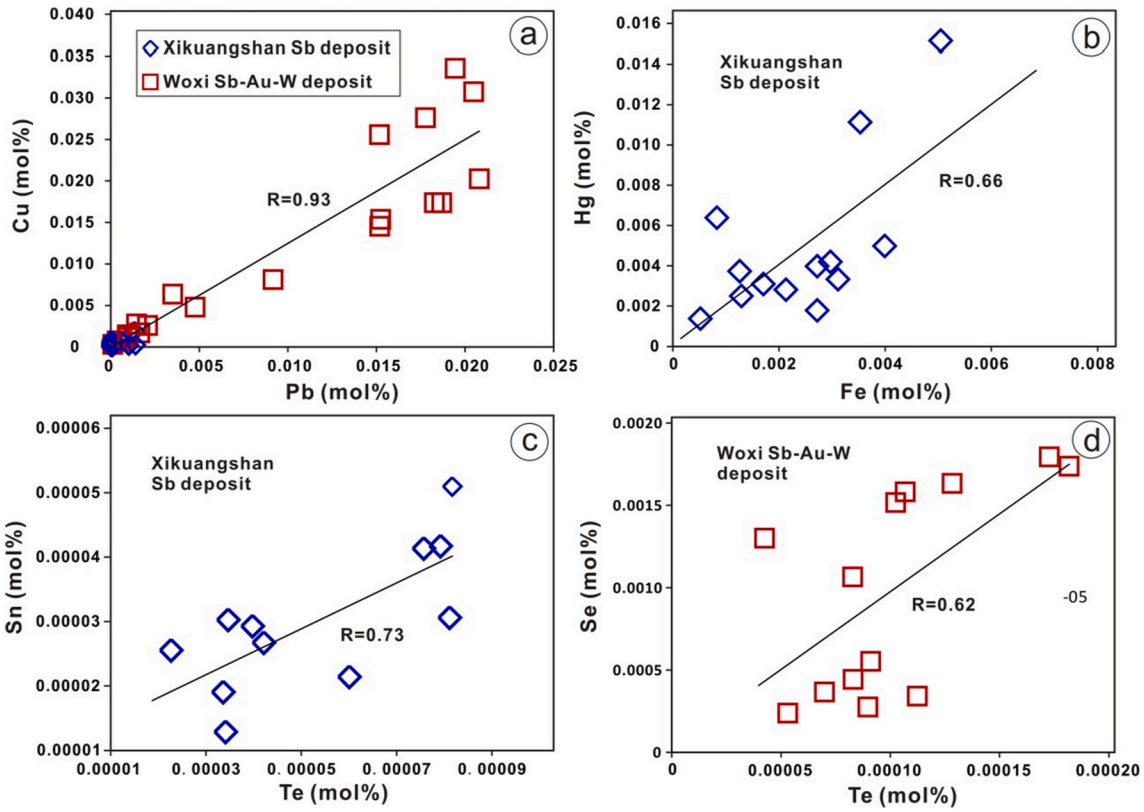

Fig. 9. Correlation plots of (a) Cu *vs.* Pb, (b) Hg *vs.* Fe, (c) Sn *vs.* Te, and (d) Se *vs.* Te in stibnite determined by LA- ICP-MS.

this study shows that stibnite from Woxi Sb deposit contains relatively high levels of base metals and As (typically at hundreds of ppm) but extremely low of Hg (from below detection limits to a few ppm). In contrast, those from the Xikuangshan Sb deposit are almost completely absent of other metals but contain measurable Hg. Such a difference in trace element composition indicates that stibnite at the two Sb deposits were generated from fluids having distinct origins.

The elevated concentrations of base metals in stibnite indicate that original Sb-bearing fluids or fluid source regions for the Woxi Sb deposit were relatively enriched in base metals (Cu, Pb). As the fluids moved upward, the changing physicochemical conditions of fluids (e.g., temperature and pH) caused the solubility of base metals to decrease and therefore base metals precipitated from the fluids prior to Sb. Experimental data suggest that chloride complexes are key ligands for base metal transport and they are stable at higher temperatures, and cooling of a hydrothermal fluid to 300 °C can destabilize and cause Cu and Pb sulfides to precipitate (Seward, 1984; Barrett and Anderson, 1988; Tagirov and Seward, 2010; Mei et al., 2015; Zhong et al., 2015). However, Sb is mainly transported as hydroxides complexes (e.g., $Sb(OH)_3$) in moderate temperature (250–300 °C) conditions (Dickson et al., 1975; Bratney, 1977; Krupp, 1988; Pokrovski et al., 2006; Obolensky et al., 2007), and a drop in temperature to below 250 °C would cause significant stibnite precipitation from fluids containing <10 ppm (Williams-Jones and Normand, 1997). Therefore, the formation of monomineralic of stibnite ores at Woxi was likely generated by cooling of an initially high-temperature hydrothermal system where Cu and Pb sulfides progressively precipitate prior to stibnite during migrating ascent. The positive correlation between Cu + Pb concentrations and sampling depth (Fig. 10a) also indicates that Cu and Pb complexes may have separated from Sb-bearing fluids at depth through precipitation of higher T sulfides during fluid ascent. Therefore, it is possible that there might be Cu and Pb mineralization at depth of the Woxi deposit. The extensive occurrence of Pb–Zn (-Cu) deposits in Woxi and adjacent districts (Li, 1996; Yang and Lao, 2007; Tang et al., 2009; Li et al., 2013) further supports this inference.

Contrastingly, the relatively low concentrations of almost all trace elements in stibnites for the Xikuangshan deposit, as well as no discernible correlation between the concentrations of Cu + Pb and sampling depth, indicate that the initial Sb-bearing fluids of this deposit were likely depleted in base and other metals, or the source regions were geochemically lacking of base metals. The minor occurrences of base metal deposits in Xikuangshan and adjacent district, in contrast to the widespread occurrence of Sb-only deposits (Tao et al., 2001; Hu et al., 2016, 2017), also support that the monomineralic nature of stibnite ores for the Xikuangshan Sb deposit may have been generated from a geochemical lack of base metals in the source regions. In addition, it should be noted that no Au mineralization is present in Xikuangshan probably because the conditions in the Devonian limestone at Xikuangshan were too oxidizing (i.e., in the field of SO_4^-) that would have favored transport of Sb but not Au (Williams-Jones and Normand, 1997), which is supported by presence of gypsum and barite at Xikuangshan. As a result, the monomineralic nature of stibnite ores for the two distinct types of Sb deposit was generated by different processes, or from different source regions.

6. Conclusions

Electron microprobe analyses did not identify any significant difference in major element compositions in stibnite, even though stibnite was collected from two deposits with different styles of mineralization (XKS-type and WX-type). However, significant differences in trace element composition were recognized between different deposit types using LA-ICP-MS analyses. In general, the Woxi deposit contains measurable concentrations of Cu, Pb, and As, whereas the Xikuangshan deposit is highly depleted in these trace elements but relatively enriched in Hg. The substitution $2Sb^{3+} \leftrightarrow Cu^{+} + Pb^{2+} + As^{3+}$ is interpreted to be the most important mechanism for the incorporation of Cu, Pb, and As within stibnite lattice. However, the difference in trace element

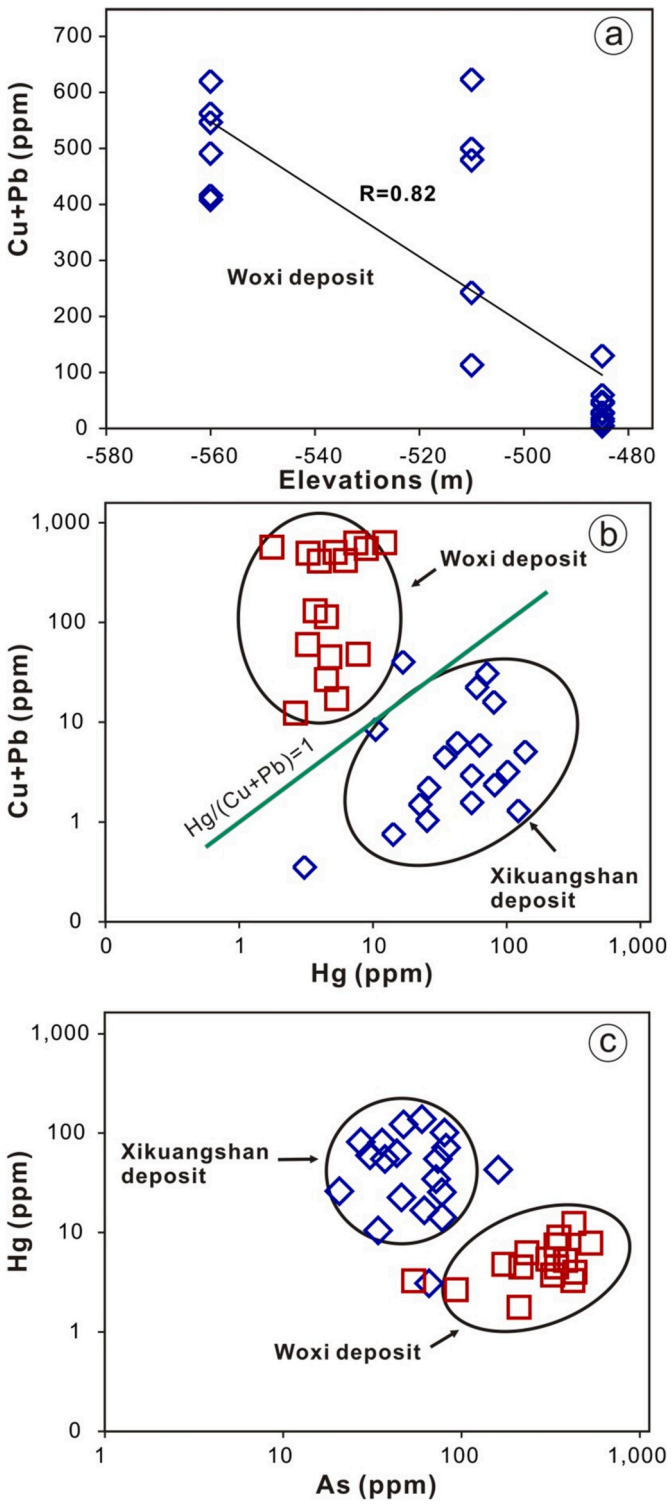

Fig. 10. Correlation plots of (a) Concentrations of Cu + Pb *vs.* Sampling depth for the Woxi deposit; (b) Hg *vs.* Cu + Pb in stibnites; the Hg/(Cu + Pb) ratio in stibnite for the Xikuangshan Sb deposit is typically greater than 1 but the Woxi deposit tends to be much lower than 1; and (c) concentrations of Hg *vs.* As in stibnites from the Xikuangshan Sb deposit and Woxi Sb–Au–W deposit.

composition in stibnite from the two major Sb deposits suggests they may have been generated from different processes or mechanisms. The Sb-bearing fluids or source regions for the Woxi deposit were relatively enriched in As and base metals, but a geochemical segregation or element partitioning by early base-metal sulfide precipitation during early fluid ascent may have led to the depletion of most other metals except antimony in higher level (thus lower T) settings resulting in the formation of nearly monomineralic stibnite ores. In contrast, there is an almost complete absence of base metals in stibnite from Xikuangshan, which we interpret was generated by a depletion of these elements in the fluid source regions. Therefore, distinct differences in trace element composition in stibnite (Fig. 10b and c) could be used to provide insights into the ore genesis or even for mineral exploration of Sb deposits.

Acknowledgements

We are grateful to Professor Michael Kersten and anonymous reviewers for their insightful comments on our manuscript. We also thank Dr. Jianping Liu for the assistance with EPMA analysis, and Dr. Zhihui Dai for the assistance with *in-situ* LA-ICP-MS trace element analysis, element mapping and cross-checking our analytical procedure. This work is supported by the projects of National Natural Science Foundation of China (41703044, 41830432, and U1812402), National Key R&D Program of China (2016YFC 0600503) and West Light Foundation of Chinese Academy of Sciences (Y7CR022000). Shanling Fu is funded by the China Scholarship Council.

Appendix A. Supplementary data

Supplementary data to this article can be found online at https://doi.org/10.1016/j.apgeochem.2020.104637.

References

Barrett, T.J., Anderson, G.M., 1988. The solubility of sphalerite and galena in 1-5M NaCl solutions to 300 °C. Geochem. Cosmochim. Acta 52, 813–820.
BGMRHN bureau of geology and mineral resource in hunan province, 1988. Regional Geology of the Hunan Province. Geological Publishing House, Beijing, pp. 286–507 (in Chinese with English summary).
Bratney, W.A., 1977. Mineralogical and Elemental Trends in the Stibnite Hill Mine Sanders County Montana. Master thesis. University of Montana, Missoula, pp. 1–123.
Chen, J., Yang, R.D., Du, L.J., Zheng, L.L., Gao, J.B., Lai, C.K., Wei, H.R., Yuan, M.G., 2018. Mineralogy, geochemistry and fluid inclusions of the Qinglong Sb-(Au) deposit, Youjiang basin (Guizhou, SW China). Ore Geol. Rev. 92, 1–18.
Chu, Y., Lin, W., Faure, M., Wang, Q.C., Ji, W.B., 2012. Phanerozoic tectonothermal events of the Xuefengshan Belt, central South China: implications from U-Pb age and Lu-Hf determinations of granites. Lithos 150, 243–255.
Ciobanu, C.L., Cook, N.J., Kelson, C.R., Guerin, R., Kalleske, N., Danyushevsky, L., 2013. Trace element heterogeneity in molybdenite fingerprints stages of mineralization. Chem. Geol. 347, 175–189.
Cook, N.J., Ciobanu, C.L., Pring, A., Skinner, W., Shimizu, M., Danyushevsky, L., Saini-Eidukat, B., Melcher, F., 2009. Trace and minor elements in sphalerite: a LA-ICPMS study. Geochem. Cosmochim. Acta 73, 4761–4791.
Cook, N.J., Ciobanu, C.L., Brugger, J., Etschmann, B., Howard, D.L., de Jonge, M.D., Ryan, C.G., Paterson, D.J., 2012. Determination of the oxidation state of Cu in substituted Cu-In-Fe-bearing sphalerite via μ-XANES spectroscopy. Am. Mineral. 97, 476–479.
Cook, N.J., Ciobanu, C.L., Giles, D., Wade, B., 2013. Correlating textures and trace elements in ore minerals. Mineral deposit research for a high-tech world. Proc. 12th Biennial SGA Meet. 288–291, 12-15 August 2013, Uppsala, Sweden.
Deditius, A.P., Utsunomiya, S., Reich, M., Kesler, S.E., Ewing, R.C., Hough, R., Walshe, J., 2011. Trace metal nanoparticles in pyrite. Ore Geol. Rev. 42, 32–46.
Dehnavi, A.S., McFarlane, C.R.M., Lentz, D.R., Walker, J.A., 2018. Assessment of pyrite composition by LA-ICP-MS techniques from massive sulfide deposits of the Bathurst Mining Camp, Canada: from textural and chemical evolution to its application as a vectoring tool for the exploration of VMS deposits. Ore Geol. Rev. 92, 656–671.
Deol, S., Deb, M., Large, R.R., Gilbert, S., 2012. LA-ICPMS and EPMA studies of pyrite, arsenopyrite and loellingite from the Bhukia-Jagpura gold prospect, southern Rajasthan, India: implications for ore genesis and gold remobilization. Chem. Geol. 326–327, 72–87.
Di Benedetto, F., Bernardini, G.P., Costagliola, P., Plant, D., Vaughan, D.J., 2005. Compositional zoning in sphalerite crystals. Am. Mineral. 90, 1384–1392.
Dickson, F.W., Radke, A.S., Weissberg, B.G., Heropoulos, C., 1975. Solid solutions of antimony, arsenic, and gold in stibnite (Sb_2S_3), Orpiment (As_2S_3), and realgar (As_2S_2). Econ. Geol. 70, 591–594.
Dill, H.G., Pertold, Z., Kilibarda, R.C., 1997. Sediment-hosted and volcanic-hosted Sb vein mineralization in the Potosi region, Central Bolivia. Econ. Geol. 92, 623–632.
Dill, H.G., Melcher, F., Botz, B., 2008. Meso- to epithermal W-bearing Sb vein-type deposits in calcareous rocks in western Thailand; with special reference to their metallogenetic position in SE Asia. Ore Geol. Rev. 34, 242–262.
Fan, D.L., Zhang, T., Ye, J., 2004. The Xikuangshan Sb deposit hosted by the Upper Devonian black shale series, Hunan, China. Ore Geol. Rev. 24, 121–133.

Fu, S.L., Hu, R.Z., Bi, X.W., Chen, Y.W., Yang, J.H., Huang, Y., 2015. Origin of triassic granites in central hunan province, South China: constraints from zircon U-Pb ages and Hf and O isotopes. Int. Geol. Rev. 57, 97–111.

Fu, S.L., Hu, R.Z., Batt, G.E., Danisik, M., Evans, N.J., Mi, X.F., 2019a. Zircon (U-Th)/He thermochronometric constraints on the mineralization of the giant Xikuangshan Sb deposit in central Hunan, South China. Miner. Deposita. https://doi.org/10.1007/s00126-019-00906-3.

Fu, S.L., Hu, R.Z., Yin, R.S., Yan, J., Mi, X.F., Song, Z.C., Sullivan, N.A., 2019b. Mercury and in situ sulfur isotopes as constraints on the metal and sulfur sources for the world's largest Sb deposit at Xikuangshan, Southern China. Miner. Deposita. https://doi.org/10.1007/s00126-019-00940-1.

Genna, D., Gaboury, D., 2015. Deciphering the hydrothermal evolution of a VMS system by LA-ICP-MS using trace elements in pyrite: an example from the bracemac-McLeod deposits, abitibi, Canada, and implications for exploration. Econ. Geol. 110, 2087–2108.

George, L., Cook, N.J., Ciobanu, C.L., Wade, B.P., 2015. Trace and minor element in galena: a reconnaissance LA-ICP-MS study. Am. Mineral. 100, 548–569.

Goh, S.W., Buckley, A.N., Lamb, R.N., Rosenberg, R.A., Moran, D., 2006. The oxidation states of copper and iron in mineral sulfides, and the oxides formed on initial exposure of chalcopyrite and bornite to air. Geochem. Cosmochim. Acta 70, 2210–2228.

Gokce, A., Spiro, B., 1994. Stable isotope study of antimony deposits in the Muratdagi region, western Turkey. Miner. Deposita 29, 361–365.

Gu, X.X., Schulz, O., Vavtar, F., Liu, J.M., Zheng, M.H., Fu, S.H., 2007. Rare earth element geochemistry of the Woxi W-Sb-Au deposit, hunan province, South China. Ore Geol. Rev. 31, 319–336.

Gu, X.X., Zhang, Y.M., Schulz, O., Vavtar, F., Liu, J.M., Zheng, M.H., Zheng, L., 2012. The Woxi W–Sb–Au deposit in Hunan, South China: an example of Late Proterozoic sedimentary exhalative (SEDEX) mineralization. J. Asian Earth Sci. 57, 54–75.

Hampton, W.A., White, G.P., Hoskin, P.W.O., Browne, P.R.L., Rodgers, K.A., 2004. Cinnabar, livingstonite, stibnite and pyrite in Pliocene silica sinter from Northland, New Zealand. Mineral. Mag. 68, 191–198.

Hinchey, J.G., Wilton, D.H.C., Tubrett, M.N., 2003. A LAM-ICP-MS study of the distribution of gold in arsenopyrite from the lodestar prospect, newfoundland, Canada. Can. Mineral. 41, 353–364.

Hu, A.X., Peng, J.T., 2016. Mesozoic lamprophyre and its origin in the Xikuangshan district, central Hunan. Acta Petrol. Sin. 32, 2041–2056 (in Chinese with English abstract).

Hu, A.X., Peng, J.T., 2018. Fluid inclusions and ore precipitation mechanism in the giant Xikuangshan mesothermal antimony deposit, South China: conventional and infrared microthermometric constraints. Ore Geol. Rev. 95, 49–64.

Hu, R.Z., Fu, S.L., Huang, Y., Zhou, M.F., Fu, S.H., Zhao, C.H., Wang, Y.J., Bi, X.W., Xiao, J.F., 2017. The giant South China Mesozoic low-temperature metallogenic domain: reviews and a new geodynamic model. J. Asian Earth Sci. 137, 9–34.

Hu, R.Z., Fu, S.L., Xiao, J.F., 2016. Major scientific problems on low-temperature metallogenesis in South China. Acta Petrol. Sin. 32, 3239–3251 (in Chinese with English abstract).

Hu, R.Z., Zhou, M.F., 2012. Multiple Mesozoic mineralization events in South China-an introduction to the thematic issue. Miner. Deposita 47, 579–588.

Hu, X.W., Pei, R.F., Zhou, S., 1996. Sm-Nd dating for antimony mineralization in the Xikuangshan deposit, Hunan, China. Resour. Geol. 4, 227–231.

Jin, J.F., 2002. Locating mechanism of superlarge antimony deposit—Xikuangshan antimony deposit example. Bull. China Soc. Mineral Petrol. Geochem. 3, 145–151 (in Chinese with English abstract).

Jin, J.F., Tao, Y., Zeng, L.J., 2001. The ore-forming fluid of Xikuangshan-type antimony deposits. Bull. China Soc. Mineral Petrol. Geochem. 3, 156–164 (in Chinese with English abstract).

Johnson, C.M., McLennan, S.M., McSween, H.Y., Summons, R.E., 2013. Smaller, better, more: five decades of advances in geochemistry. In: Bickford, M.E. (Ed.), The Web of Geological Sciences: Advances, Impacts, and Interactions, vol. 500. Geological Society of America Special Papers, pp. 259–302.

Krupp, R.W., 1988. Solubility of stibnite in hydrogen sulfide solutions, speciation, and equilibrium constants, from 25 to 350°C. Geochem. Cosmochim. Acta 52, 3005–3015.

Kuang, W.L., 2000. Research on the metallogenic model of Xikuangshan superlarge antimony deposit. World Geol. 19, 26–30 (in Chinese with English abstract).

Large, R.R., Danyushevsky, L., Hollit, C., Maslennikov, V., Meffre, S., Gilbert, S., Bull, S., Scott, R., Emsbo, P., Thomas, H., 2009. Gold and trace element zonation in pyrite using a laser imaging technique: implications for the timing of gold in orogenic and Carlin-style sediment-hosted deposits. Econ. Geol. 104, 635–668.

Li, H., Wu, Q.H., Evans, N.J., Zhou, Z.K., Kong, H., Xi, X.S., Lin, Z.W., 2018. Geochemistry and geochronology of the Banxi Sb deposit: implications for fluid origin and the evolution of Sb mineralization in central-western Hunan, South China. Gondwana Res. 55, 112–134.

Li, K., Liu, K., Tang, C.Y., Duan, Q.F., 2013. Characteristics of zinc geochemical blocks and assessment of zinc resource potential in western Hunan and eastern Guizhou Province. Chin. Geol. 40, 1270–1277 (in Chinese with English abstract).

Li, S.S., 1996. Evolution of antimony mineralization by the mantle plume of deep fluid in central Hunan. Hunan Geol. 15, 137–142 (in Chinese with English abstract).

Liang, Y., Wang, G.G., Liu, S.Y., Sun, Y.Z., Huang, Y.G., Hoshino, K, 2014. A Study on the Mineralization of the Woxi Au–Sb–W Deposit, Western Hunan, China. Resource Geology 65, 27–38.

Liu, G.M., Jian, H.M., 1983. Geological characteristics of the Xikuangshan antimony ore field. Miner. Deposits 2, 43–49 (in Chinese with English abstract).

Liu, H.P., Zhang, Y.L., Hu, W.Q., 1985. A study on the origin of the Xikuangshan antimony deposit, Hunan. Hunan Geol. 4, 28–39 (in Chinese with English abstract).

Luo, X.L., Yi, S.J., Liang, J.C., 1984. On the genesis of the Woxi Au-Sb-W deposit, W-Hunan. Geol. Explor. 20, 1–10 (in Chinese).

Ma, D.S., Pan, J.Y., Xie, Q.L., 2003. Ore sources of Sb (Au) deposits in Center Hunan: II. Evidence of isotopic geochemistry. Mineral Deposits 21, 78–87.

Ma, D.S., Pan, J.Y., Xie, Q.L., He, J., 2002. Ore source of Sb (Au) deposits in Center Hunan: I. Evidences of trace elements and experimental geochemistry. Miner. Deposits 3, 366–376 (in Chinese with English abstract).

Mao, J.W., Li, H.Y., 1997. Research on genesis of the gold deposits in the Jiangnan Terrain. Geochemica 26, 71–81.

Mei, Y., Sherman, D.M., Liu, W.H., Etschmann, B., Testemale, D., Brugger, J., 2015. Zinc complexation in chloride-rich hydrothermal fluids (25–600°C): a thermodynamic model derived from ab initio molecular dynamics. Geochem. Cosmochim. Acta 150, 265–284.

Murao, S., Sie, S.H., Hu, X., Suter, G.F., 1999. Contrasting distribution of trace elements between representative antimony deposits in southern China. Nucl. Instrum. Methods Phys. Res. B 150, 502–509.

Obolensky, A.A., Gushchina, L.V., Borisenko, A.S., Borovikov, A.A., Pavlova, G.G., 2007. Antimony in hydrothermal processes solubility, conditions of transfer ad metal-bearing capacity of solutions. Russ. Geol. Geophys. 48, 992–1001.

Peng, B., Frei, R., 2004. Nd-Sr-Pb isotopic constraints on metal and fluid sources in W-Sb-Au mineralization at Woxi and Liaojiaping (Western Hunan, China). Miner. Deposita 39, 313–327.

Peng, J.T., Hu, R.Z., Burnard, P.G., 2003a. Samarium-neodymium isotope systematics of hydrothermal calcite from the Xikuangshan antimony deposit (Hunan, China): the potential of calcite as a geochronometer. Chem. Geol. 200, 129–136.

Peng, J.T., Hu, R.Z., Zhao, J.H., Fu, Y.Z., Lin, Y.X., 2003b. Scheelite Sm-Nd dating and quartz Ar-Ar dating for Woxi Au-Sb-W deposit, western Hunan. Chin. Sci. Bull. 48, 2640–2646.

Pearce, N.J., Perkins, W.T., Westgate, J.A., Gorton, M.P., Jackson, S.E., Neal, C.R., Chenery, S.P., 1997. A compilation of new and published major and trace element data for NIST SRM 610 and NIST SRM 612 glass reference materials. Geostand. Newsl. 21, 115–144.

Pokrovski, G.S., Borisova, A.Y., Roux, J., Hazemann, J.L., Petdang, A., Tella, M., Testemale, D., 2006. Antimony speciation in saline hydrothermal fluids: a combined X-ray absorption fine structure spectroscopy and solubility study. Geochem. Cosmochim. Acta 70, 4196–4214.

Qiu, L., Yan, D.P., Tang, S.L., Wang, Q., Yang, W.X., Tang, X.L., Wang, J.B., 2016. Mesozoic geology of southwestern China: indosinian foreland overthrusting and subsequent deformation. J. Asian Earth Sci. 122, 91–105.

Reich, M., Deditius, A., Chryssoulis, S., Li, J.W., Ma, C.Q., Parada, M.A., Barra, F., Mittermayr, F., 2013. Pyrite as a record of hydrothermal fluid evolution in a porphyry copper system: a SIMS/EMPA trace element study. Geochem. Cosmochim. Acta 104, 42–62.

Rytuba, J.J., 2003. Mercury from mineral deposits and potential environmental impact. Environ. Geol. 43, 326–338.

Seward, T.M., 1984. The formation of lead (II) chloride complexes to 300°C: a spectrophotometric study. Geochem. Cosmochim. Acta 48, 121–134.

Shao, J.B., Wang, P., Chen, D.Z., 1996. Mineralogical studies on pyrites in Woxi Au-Sb-W deposit, western Hunan. Hunan Geol. 15, 26–33 (in Chinese with English abstract).

Shi, M.K., Fu, B.Q., Jin, X.X., 1993. Antimony Metallogeny in Central Part of Hunan Province. Hunan Press of Science and Technology, Changsha, pp. 1–151 (in Chinese).

Stanton, R.L., 1972. Ore Petrology. McGraw-Hill Book, New York, N.Y., pp. 1–713

Tao, Y., Gao, Z.M., Jin, J.F., Zeng, L.J., 2001. The origin of ore-forming fluid of Xikuangshan-type antimony deposits in central Hunan province. Geol. Geochem. 29, 14–20 (in Chinese with English abstract).

Tao, Y., Gao, Z.M., Jin, J.F., Zeng, L.J., 2002. Ore-forming conditions of Xikuangshan-type antimony deposits in central Hunan. Earth Sci. 2, 184–195 (in Chinese with English abstract).

Tang, C.Y., Duan, Q.F., Zou, X.W., Li, K., 2009. Preliminary approach on the Stratabound Lead-Zinc deposits and lithofacies palaeogeographic framework of the Dengyingxia age, Sinian (Ediacaran), in western Hunan-western Hubei area. Geol. Rev. 55, 673–683 (in Chinese with English abstract).

Tagirov, B.R., Seward, T.M., 2010. Hydrosulfide/sulfide complexes of zinc to 250 °C and the thermodynamic properties of sphalerite. Chem. Geol. 269, 301–311.

Watling, R.J., Herbert, H.K., Abell, I.D., 1995. The application of laser ablation-inductively coupled plasma mass spectrometry (LA-ICP-MS) to the analysis of selected sulfide minerals. Chem. Geol. 124, 67–81.

Williams-Jones, A.E., Normand, C., 1997. Controls of mineral parageneses in the system Fe- Sb-S-O. Econ. Geol. 92, 308–324.

Wilson, S.A., Ridley, W.I., Koenig, A.E., 2002. Development of sulfide calibration standards for the laser ablation inductively-coupled plasma mass spectrometry technique. JAAS (J. Anal. At. Spectrom.) 406–409.

Wilson, S.C., Lockwood, P.V., Ashley, P.M., Tighe, M., 2010. The chemistry and behaviour of antimony in the soil environment with comparisons to arsenic: a critical review. Environ. Pollut. 158, 1169–1181.

Wu, J.D., 1993. Antimony vein deposits of China. Ore Geology Reviews 8, 213–232.

Wu, L.S., Hu, X.W., 2000. Xikuangshan mica-plagioclase lamprophyre and its granite inclusions, Hunan Province. Geol. Geochem. 28, 51–55 (in Chinese with English abstract).

Xie, G.Q., Peng, J.T., Hu, R.Z., Jia, D.C., 2001. Geological characteristics of lamprophyres in the Xikuangshan antimony ore deposits, Hunan province. Acta Petrol. Sin. 17, 629–636 (in Chinese with English abstract).

Xie, G.Q., Mao, J.W., Li, W., Fu, B., Zhang, Z.Y., 2019. Granite-related Yangjiashan tungsten deposit, southern China. Miner. Deposita 54, 67–80.

Yang, D.S., Shimizu, M., Shimazaki, H., Li, X.H., Xie, Q.L., 2006a. Sulfur isotope geochemistry of the supergiant Xikuangshan Sb deposit, central Hunan, China: constraints on sources of ore constituents. Resour. Geol. 56, 385–396.
Yang, R.Y., Ma, D.S., Bao, Z.Y., Pan, J.Y., Cao, S.L., Xia, F., 2006b. Geothermal and fluid flowing simulation of ore-forming antimony deposits in Xikuangshan. Sci. China, Ser. A 8, 862–871.
Yang, S.X., Lao, K.T., 2007. Geological characteristics and ore indicators of lead-zinc deposits in northwestern Hunan, China. Geol. Bull. China 26, 899–908 (in Chinese with English abstract).
Yao, J.L., Shu, L.S., Cawood, P.A., Li, J.Y., 2016. Delineating and characterizing the boundary of the Cathaysia block and the jiangnan orogenic belt in south China. Precambrian Res. 275, 265–277.
Zhao, J.H., Zhou, M.F., Yan, D.P., Zheng, J.P., Li, J.W., 2011a. Reappraisal of the ages of Neoproterozoic strata in South China: no connection with the Grenvillian orogeny. Geology 39, 299–302.
Zhao, H.X., Frimmel, H.E., Jiang, S.Y., Dai, B.Z., 2011b. LA-ICP-MS trace element analysis of pyrite from the Xiaoqinling gold district, China: implications for ore genesis. Ore Geol. Rev. 43, 142–153.
Zeng, G.P., Gong, Y.J., Wang, Z.F., Hu, X.L., Xiong, S.F., 2017. Geology, fluid inclusions, and geochemistry of the Zhazixi Sb–W deposit, Hunan, South China. Ore Geology Reviews 91, 1025–1039.
Zeng, G.P., Gong, Y.J., Wang, Z.F., Hu, X.L., Xiong, S.F., 2017. Structures of the Zhazixi Sb–W deposit, South China: Implications for ore genesis and mineral exploration. Journal of Geochemical Exploration 182, 10–21.
Zhang, J., Li, L., Gilbert, S., Liu, J.J., Shi, W.S., 2014. LA-ICP-MS and EPMA studies on the Fe-S-As minerals from the Jinlongshan gold deposit, Qinling Orogen, China: implications for the ore-forming processes. Geol. J. 49, 482–500.
Zhong, R.C., Brugger, J., Chen, Y.J., Li, W.B., 2015. Contrasting regimes of Cu, Zn and Pb transport in ore-forming hydrothermal fluids. Chem. Geol. 395, 154–164.
Zhu, Y.N., Peng, J.T., 2015. Infrared microthermometric and noble gas isotope study of fluid inclusions in ore minerals at the Woxi orogenic Au–Sb–W deposit, western Hunan, South China. Ore Geol. Rev. 65, 55–69.